RAA 2016 Vol. **16** No. **9**, 139 (14pp) doi: 10.1088/1674–4527/16/9/139
http://www.raa-journal.org *http://iopscience.iop.org/raa*

***R**esearch in*
***A**stronomy and*
***A**strophysics*

The point spread function reconstruction by using Moffatlets – I

Bai-Shun Li[1,2], Guo-Liang Li[1], Jun Cheng[3], John Peterson[3] and Wei Cui[3]

[1] Purple Mountain Observatory, Chinese Academy of Sciences, Nanjing 210008, China; *guoliang@pmo.ac.cn*
[2] University of Chinese Academy of Sciences, Beijing 100049, China
[3] Department of Physics, Purdue University, 525 Northwestern Ave, West Lafayette, Indiana 47907, USA

Received 2016 March 1; accepted 2016 April 24

Abstract Shear measurement is a crucial task in current and future weak lensing survey projects. The reconstruction of the point spread function (PSF) is one of the essential steps involved in this process. In this work, we present three different methods, Gaussianlets, Moffatlets and Expectation Maximization Principal Component Analysis (EMPCA), and quantify their efficiency on PSF reconstruction using four sets of simulated Large Synoptic Survey Telescope (LSST) star images. Gaussianlets and Moffatlets are two different sets of basis functions whose profiles are based on Gaussian and Moffat functions respectively. EMPCA is a statistical method performing an iterative procedure to find the principal components (PCs) of an ensemble of star images. Our tests show that: (1) Moffatlets always perform better than Gaussianlets. (2) EMPCA is more compact and flexible, but the noise existing in the PCs will contaminate the size and ellipticity of PSF. By contrast, Moffatlets keep the size and ellipticity very well.

Key words: cosmology: observations — stars: imaging — techniques: image processing

1 INTRODUCTION

Gravitational lensing provides a unique way to map the matter distribution in the Universe. By measuring the shape distortion of distant galaxies, one can gain the lensing signals and thus study the mass distribution in clusters of galaxies (Mellier 1999) and large scale structures (Refregier 2003b; Van Waerbeke et al. 2013; Planck Collaboration et al. 2014), as well as directly probe the invisible dark sector and fundamental nature of gravity (Hoekstra & Jain 2008; Massey et al. 2010; Huterer 2010; Moffat 2006). However, the shape of a galaxy can be distorted by several different mechanisms, such as (1) shear by lensing effect, (2) convolution with the point spread function (PSF), (3) pixelation on a CCD and (4) effects from noise. In order to accurately recover the original galaxy shape (shape right after the galaxy is lensed), decrease statistical error and quantify the intrinsic alignments of background galaxies (Bartelmann & Schneider 2001), a number of current and planned large-area surveys have been proposed, such as Euclid (Laureijs et al. 2011), the Large Synoptic Survey Telescope (LSST)[1](LSST Science Collaboration et al. 2009), and WFIRST-AFTA (Spergel et al. 2015), to reduce the statistical uncertainty. On the other hand, a variety of weak lensing shear measurement algorithms (Kaiser et al. 1995; Luppino & Kaiser 1997; Hoekstra et al. 1998; Refregier & Bacon 2003) have been proposed and a series of data analysis challenges, such as GREAT08 (Bridle et al. 2010), GREAT10 (Kitching et al. 2012, 2013) and the most recent one GREAT3[2,3](Mandelbaum et al. 2014), have been carried out to improve precision and reduce systematic biases.

One of the crucial parts in reducing the systematic biases in shear measurement is modeling the PSF to adequate precision. The scatter and systematic bias in the size and ellipticity of the reconstructed PSF will introduce systematic bias to the shear measurement (Paulin-Henriksson et al. 2008, 2009; Massey et al. 2013). PSF is the spreading of light caused by various complex physical processes, such as diffraction by the aperture of the telescope, imperfect optics and tracking systems, temperature variations in the camera, vibrations, optical changes during telescope refocusing, and turbulence in the atmosphere (a concern for ground-based telescopes). This means that the PSF cannot be represented in the form of a simple explicit function. A Gaussian PSF has usually been assumed to serve as a good approximation for most astronomical cases. However, it deviates from a real PSF due to the existence of "wings" in stellar profiles. The Moffat function is shown to describe well the presence of wings (when the value of β is taken properly) and contains the Gaussian function as a limiting case (when $\beta \to \infty$) (Trujillo et al. 2001). However to reproduce the PSF with the precision needed for weak lensing studies, high-order correction is required. A technique called Shapelets (Refregier 2003a;

[1] *http://www.lsst.org*

[2] *http://great3challenge.info*

[3] *http://great3.projects.phys.ucl.ac.uk/leaderboard/*

Refregier & Bacon 2003; Massey & Refregier 2005) decomposes an object using a series of localized basis functions and compresses the information about the shape into a small number of expansion coefficients. In this paper, we use the Gaussian and Moffat functions as primary profiles to create two basis function sets which we call Gaussianlets and Moffatlets (Li et al. 2013) respectively to decompose the PSF.

A minimum of 50 stars is needed for the PSF to be calibrated in order to control the systematic errors to a level similar to the statistical errors that have been estimated for ambitious future surveys (Paulin-Henriksson et al. 2008). With this ensemble of stars in an image, a set of principal components (PCs) can be solved via the statistical procedure called principal component analysis (PCA). In Bailey (2012), a framework called expectation maximization PCA (EMPCA) is introduced that extends classical PCA to a form that can incorporate estimates of measurement variance while solving for the PCs. In this paper, we use this method to find the PCs of a PSF.

This article is organized as follows. In Section 2 we describe the three methods, Gaussianlets, Moffatlets and EMPCA, and their algorithms for reconstructing PSFs. In Section 3 we describe the simulated structure of the data we use. In Section 4 we perform numerical tests of our three methods and compare their reconstruction efficiency. Finally, we conclude by discussing the limitations and prospects of our algorithm in Section 5.

2 RECONSTRUCTION METHODS

2.1 Gaussianlets and Moffatlets

The so-called Gaussianlets method we use here is a reduced version of shapelets (Massey & Refregier 2005) where we only keep the basis functions with $m = 0$. The explicit mathematical formula of Gaussianlets is

$$P_l(r) = \frac{1}{\sqrt{\pi\sigma_d^2}} e^{-\frac{r^2}{2\sigma_d^2}} L_l\Big(\frac{r^2}{\sigma_d^2}\Big). \quad (1)$$

The basis functions in Moffatlets are also circularly symmetric and contain no angular components. The formula (see Appendix A for more details) is

$$Q_l(r) = \sqrt{\frac{2\beta-1}{\pi r_d^2}} L_l[v(r)]\Big[1+\Big(\frac{r}{r_d}\Big)^2\Big]^{-\beta}, \quad (2)$$

where

$$v(r) = \Big(\frac{1}{2\beta}-1\Big)\ln\Big[1+\Big(\frac{r}{r_d}\Big)^2\Big]^{-2\beta}. \quad (3)$$

In both Equations (1) and (2), $L_l(x)$ is the Laguerre polynomial

$$L_l(x) = \frac{e^x}{l!}\frac{d^l}{dx^l}\Big(e^{-x}x^l\Big) = \frac{1}{l!}\Big(\frac{d}{dx}-1\Big)^l x^l. \quad (4)$$

where l runs from 0 to ∞. Mathematically, both sets of basis functions are orthogonalized and normalized in the following sense,

$$\int_0^{+\infty} P_l(r)P_m(r)dr = \int_0^{+\infty} Q_l(r)Q_m(r)dr = \delta_{lm}. \quad (5)$$

There are free parameters (σ_d in Gaussianlets and (β, r_d) in Moffatlets) that are adjustable in the basis functions. Tuning their values, we can change the size and steepness of radial variation in the basis functions. In the process of modeling, these free parameters are adjusted to the values that best fit the data, which means the shape of the 0th order function most closely fits the averaged shape of a set of stellar profiles. With this strategy, the expansion is ensured to be very compact.

Using these basis functions, we can reproduce the star images as follows:

(1) Calculate the center and ellipticity for each stellar profile using the fast fitting algorithms (Li et al. 2012).
(2) According to the center and ellipticity of each star, the shape parameters of the Gaussian and Moffat model are also calculated using the fast fitting algorithm (see Li et al. 2012). Trujillo et al. (2001) argued that a Moffat function could be used to reliably model the turbulence prediction when $\beta \sim 4.765$. However, the PSFs usually measured in real images have bigger "wings," or equivalently smaller values of β ($2.5 < \beta < 4$; see Saglia et al. 1993), than those expected from turbulence theory. In this paper, we simply set $\beta = 3.5$.
(3) Calculate the mean of the best-fitting parameters over all stars, and use the mean as the value of parameter(s) in the basis functions to create a set of basis functions we will then use.
(4) Finally for each star image, we squeeze the circularly symmetric basis functions to the same ellipticity as the star has by performing a coordinate transformation and then decompose the star image into several elliptical basis functions. The basis functions have to be pixelated on a finite region in order to perform the associated numerical simulation. This causes violation of the orthogonality and the coefficients of each basis function cannot be simply derived from an inner product. We overcome this difficulty by solving a maximum likelihood solution (e.g., Andrae et al. 2011).

Finally, we have two parameters (e_1, e_2) and several coefficients of basis functions for each star. The first eight basis functions of Gaussianlets (first row) and Moffatlets (second row) are shown in Figure 1. We can see that Moffatlets are more extended than Gaussianlets. This property will lead the Moffatlets method to show good performance in the reconstruction of the star image.

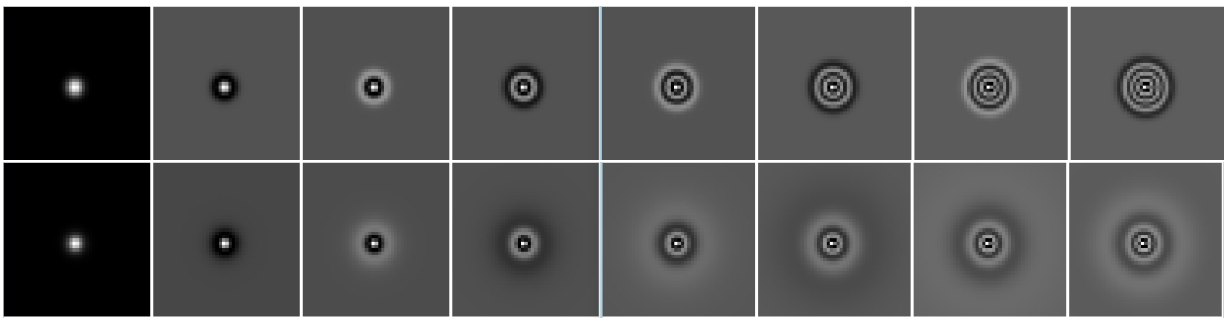

Fig. 1 A demonstration of the first eight basis functions of Gaussianlets (*first row*) and Moffatlets (*second row*) constructed by the program. From left to right, as the order of the basis functions increases, the number of "circles" increases. As you will also notice, Moffatlets basis functions are "fatter" than Gaussianlets basis functions.

2.2 EMPCA

The EMPCA method is an extended version of the classical PCA. It uses expectation (E-step) and maximization (M-step) to subtract the eigenvectors. The most important improvement is that noise in the data can also be taken into account (Bailey 2012). These improvements provide a high-efficiency calculation and reasonable handling of noise. We adopt a per-variable weighting strategy in this work, which can be summarized as follows. The χ^2 function is defined as

$$\chi^2 = \sum_{\mathrm{var}i,\ \mathrm{obs}j} w_{ij}(A_{ij} - \phi_i c_j)^2. \tag{6}$$

For given eigenvector ϕ, the E-step gives the optimal coefficient as

$$c_j \longleftarrow \frac{\sum_i w_{ij} A_{ij}}{\sum_i w_{ij}\phi_i^2}, \tag{7}$$

Then the M-step improves estimation of the eigenvector as

$$\phi_i \longleftarrow \frac{\sum_j w_{ij} c_j A_{ij}}{\sum_j w_{ij} c_j^2}. \tag{8}$$

Here $A_{ij} = (a_1, \ldots, a_{\mathrm{Nstar}})$ is the dataset in which a_j is a vector denoting the jth star, ϕ_i is the initial estimation of the 1st PC we are searching for and c_j is the coefficient calculated by projecting the jth star on the PC. The goal is to solve the minimization problem of Equation (6) incorporating a weight matrix w_{ij}. The algorithm starts with an arbitrary ϕ, and iteratively updates ϕ through the E-step and M-step until convergence. To find higher-order PCs, we replace A by $(A - \phi c)$ and repeat the above process. This procedure can be continued until no more effective PCs are present.

The weight is simply related to the noise in each pixel as $w_{ij} = 1/\sigma_{ij}^2$. Our simulated stars contain Poisson and Gaussian noise. The estimation of σ_{ij} is given by the following rule: Gaussian noise σ is evaluated on the outskirt of each star image, then for pixels with value I smaller than 2σ, we take $\sigma_{ij} = \sigma$; for pixel value I larger than 2σ, we take $\sigma_{ij} = \sqrt{\sigma^2 + gI}$, where g is the gain of the CCD.

3 DATA DESCRIPTION

In this paper, we invoke PhoSim (Peterson et al. 2015), our primary tool for generating simulated images. PhoSim uses a photon Monte Carlo approach to construct images by sampling photons from models of astronomical source populations. PhoSim is designed to represent LSST performance and generates images expected for LSST with high fidelity. All detailed atmosphere, telescope and camera physical effects that determine the shapes, locations and brightnesses of individual stars and galaxies can be accurately represented. This makes PhoSim a perfect simulation tool for study of the PSF.

To examine the PSF effects, four images are generated using PhoSim version 3.4. We simulate images for two LSST chips: R22S11 denotes a chip in the center of the focal plane while R02S01 denotes a chip near the edge of the focal plane. In PhoSim, all the physical effects can be separately turned 'on' and 'off' so that we can have control over the effects which may affect the PSF. Two of the images are simulated with diffraction 'off' and the other two with diffraction 'on.' For all the other physical effects, default settings of LSST are used.

In the four images, the pixel size is $0.2''$ pixel^{-1} and the pixel values are simulated in ADU unit with gain$= 1$, hence the value on each pixel counts the number of photons falling in it. The star images only contain Poisson noise and all have roughly the same magnitude. We can then add different amounts of background Gaussian noise to each star and estimate the signal-to-noise ratio (SNR) within a 10×10 square around the brightest pixel by using the definition $\mathrm{SNR} = \Sigma_{\mathrm{p}}(I_{\mathrm{p}})/\sqrt{\Sigma_{\mathrm{p}}(\sigma^2 + I_{\mathrm{p}})}$, where I_{p} is the simulated LSST data with only Poisson noise and σ is the Gaussian noise we add later.

Based on our simulation, an explicit model fitting is also performed as a verification of the result in Trujillo et al. (2001). They claimed that the Moffat function is a better model for fitting PSFs than the Gaussian function. We choose several bright stars from our simulation and then fit them with these two models by minimizing the χ^2

function

$$\chi^2 = \sum_{i,j} \frac{(I^0_{ij} - F_{ij})^2}{\sigma^2_{ij}}, \qquad (9)$$

where F_{ij} is the fitting function and σ_{ij} is the Possion noise in each pixel.

Figure 2 shows the fitted brightness profile along the diagonal for our four kinds of simulated stars. Clearly, the Moffat model can fit our simulated stars much better than the Gaussian profile. The Gaussian profile only fits the inner part well but drops too fast in the outer region. Moreover, the fitting of the Moffat model is well behaved even at large radius. Therefore, we would expect that Moffatlets will also work better than Gaussianlets in the following tests.

One hundred stars are randomly selected from each CCD. The test is then divided into four cases: In the first three cases, a uniform level of Gaussian noise is added to the 100 stars with $\sigma = 10$, 40 and 80 (with $\langle \mathrm{SNR} \rangle \approx 416,\ 232$ and 132 respectively); in the fourth case, different amounts of Gaussian noise with the value of σ randomly ranging from 10 to 100 are added to the stars (this case will be denoted as "ran (10–100)" later in this article). By including the last case, we try to mimic 100 stars with different SNRs ($80 \lesssim \mathrm{SNR} \lesssim 500$), or in terms of observations, there are 100 stars with different magnitudes. Figure 3 shows these four cases of R02S01-diffraction-OFF simulation.

4 RESULTS

The reconstructions using the three methods are performed on data that are affected by noise in all four cases. We aim to test how efficient these three methods are and how the noise affects the results. For the basis function methods, the shape parameters are computed according to the average shapes of the 100 stars. The values of σ_d and r_d in the Gaussianlets and Moffatlets are listed in Table 1 and Table 2 respectively. These show that the values of σ_d and r_d taken for "diffraction on" data are larger those of "diffraction off" data. This is because spikes exist in "diffraction on" data and make the stars more extended. Once the parameters are fitted, we can create the basis functions. Figure 1 demonstrates the first eight basis functions for both Gaussianlets and Moffatlets.

Noise affects the EMPCA method in a very apparent way. In Figure 4, a set of patterns are clearly resolved by the PCA algorithm in case 1 ($\sigma = 10$). But as more noise is added, less useful PCs will be extracted. As shown in case 2 ($\sigma = 40$), case 3 ($\sigma = 80$) and case 4 ($\sigma =$ ran (10–100)), all the higher-order PCs contain visible noise and no signal can even be easily recognized in some of them. This introduces uncertainty when choosing the appropriate number of PCs to be used in the EMPCA method.

Table 1 Value of σ_d taken in Different Simulation Runs

	10	40	80	ran (10–100)
R02S01-diffraction-OFF	1.419150	1.419232	1.419417	1.419747
R02S01-diffraction-ON	1.906670	1.904350	1.904945	1.906408
R22S11-diffraction-OFF	1.443192	1.442398	1.442060	1.440537
R22S11-diffraction-ON	1.921579	1.919953	1.920336	1.921725

Table 2 Value of r_d taken in Different Simulation Runs

	10	40	80	ran (10–100)
R02S01-diffraction-OFF	3.030692	3.029967	3.029196	3.029439
R02S01-diffraction-ON	4.061016	4.052640	4.051725	4.054829
R22S11-diffraction-OFF	3.083501	3.080003	3.077113	3.072700
R22S11-diffraction-ON	4.094765	4.089887	4.085220	4.086687

Here we introduce the usual χ^2 function to quantify how well the reconstruction is done.

$$\chi^2 = \sum_{i,j} \frac{\left(I^0_{ij} - I^{(\mathrm{reconstructed})}_{ij}\right)^2 w_{ij}}{N_{\mathrm{pixels}}}. \qquad (10)$$

I^0 refers to the original extracted star with only Poisson noise. The weight is the same as we employed in the EMPCA algorithm.

We draw the χ^2-curves corresponding to reconstructions using a different number of PCs (Fig. 5). (The reconstruction is performed on image R02S01-diffraction-OFF, $\sigma = 40$.) The green line which corresponds to using three PCs is the lowest. As we decrease the number of PCs used, the χ^2-curve increases in height (as the black line representing one PC indicates) since fewer PCs mean less information is taken into account. As we increase the number of PCs that are used, the χ^2-curve also increases in height due to the fact that more noise is contained in the reconstructed star images. In fact, we can see that using seven PCs is worse than just using one PC. In the following reconstructions, applied to all data sets, we always use four PCs.

As for our basis function methods, we expect a larger number of free parameters because the theoretical basis functions cannot be more compact than the numerically solved PCs. Since there are already two parameters (e_1, e_1) for each star, we simply adopt four basis functions for the Moffatlets and Gaussianlets method.

Using the quantity χ^2, the three methods are compared for all data sets in Figures 6, 7, 8 and 9, where the blue, red and green lines represent the results of EMPCA, Moffatlets and Gaussianlets respectively. All of these results broadly support the same conclusions:

(1) EMPCA always performs better than Moffatlets and Gaussianlets for the high SNR cases. This is because there are high-order patterns of brightness distributions in star images which cannot be described by our elliptical basis functions but can be resolved by EMPCA. But for the low SNR cases, the results of EMPCA are comparable with the results of Moffatlets.

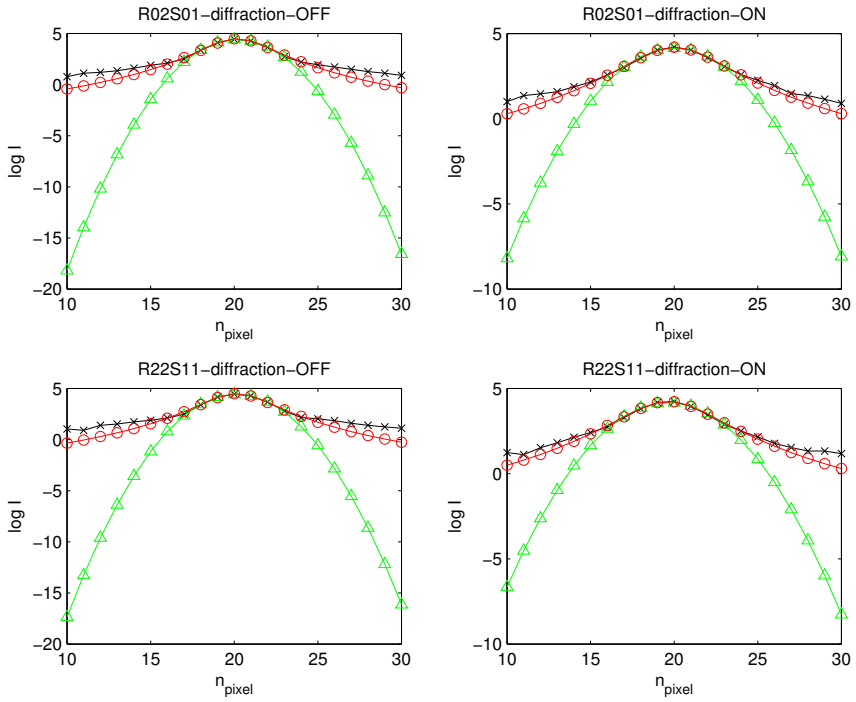

Fig. 2 After computing the best fits for parameters σ and r_d, we construct the corresponding Gaussian (*green triangles and lines*) and Moffat (*red circles and lines*) functions and compare to the original star profiles (*black crosses and lines*). The drawn curves are only the cross-sections of the 2-dimensional images (*Color version is online*).

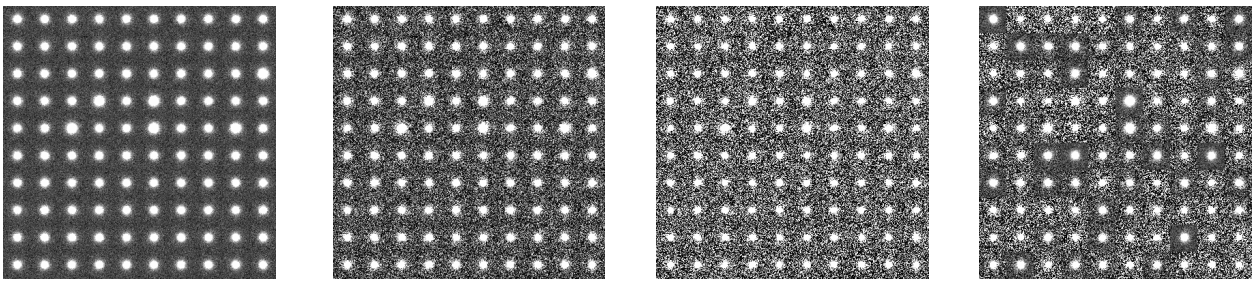

(a) $\sigma = 10$ (b) $\sigma = 40$ (c) $\sigma = 80$ (d) $\sigma =$ ran (10–100)

Fig. 3 The four panels show background noise added in four different cases. All pictures are drawn according to the same gray scale.

(2) Moffatlets are always better than Gaussianlets. As mentioned in the introduction and also in Trujillo et al. (2001), a Moffat function fits a real PSF better than a Gaussian function. Gaussianlets perform especially poorly in case 1 since the Gaussian function cannot describe the presence of large "wings" in a PSF which are not buried by noise. Several high peaks indicated by the green line in case 4 (σ = run (10–100)) correspond to stars with higher SNRs. We also see the "diffraction on" stars can be reconstructed better than "diffraction off" stars. This is because in our simulation, diffraction spikes are not very sharp, but rather they make the stars more extended and smooth some high order minor substructures.

Another two quantities are also introduced to serve as tests for the efficiency of the reconstructions. The first quantity is the ellipticity, which is defined as:

$$e_1 = \frac{Q_{11} - Q_{22}}{Q_{11} + Q_{22}}, \tag{11}$$

$$e_2 = \frac{2Q_{12}}{Q_{11} + Q_{22}}. \tag{12}$$

where Q_{ij} are second brightness moments of a star image. A Gaussian filter is employed in calculating the moments. The full width at half maximum (FWHM) of the Gaussian filter is the mean FWHM of stars.

The other quantity is the square rms size of a star, defined as

$$R^2 = Q_{11}^2 + Q_{22}^2. \tag{13}$$

Using these formulas, we first measure (R^2, e_1, e_2) for the original stars without Gaussian noise added yet. Then, we calculate (R^2, e_1, e_2) for the reconstructed stars in each

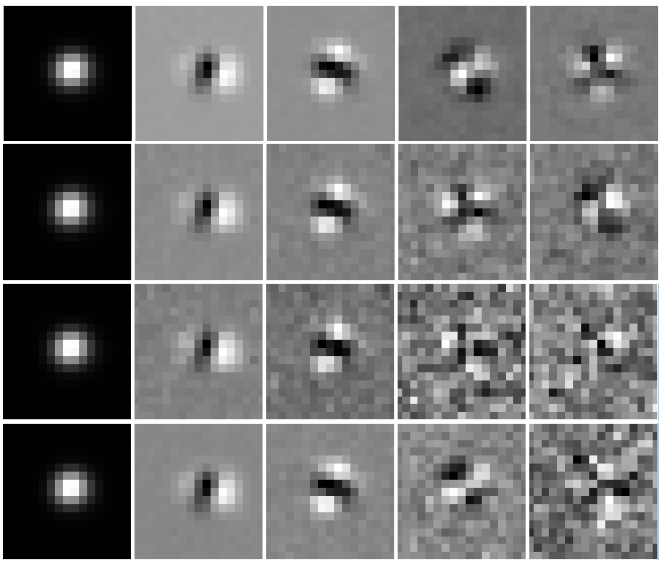

Fig. 4 The first five PCs extracted in different cases. The first row is the case in which we add Gaussian noise with $\sigma = 10$ to the data. In this case, we can see the most amount of signals. The other three rows are cases of $\sigma = 40, 80$ and ran (10–100) respectively. As the noise increased, less and less signal can be recognized in the higher order PCs.

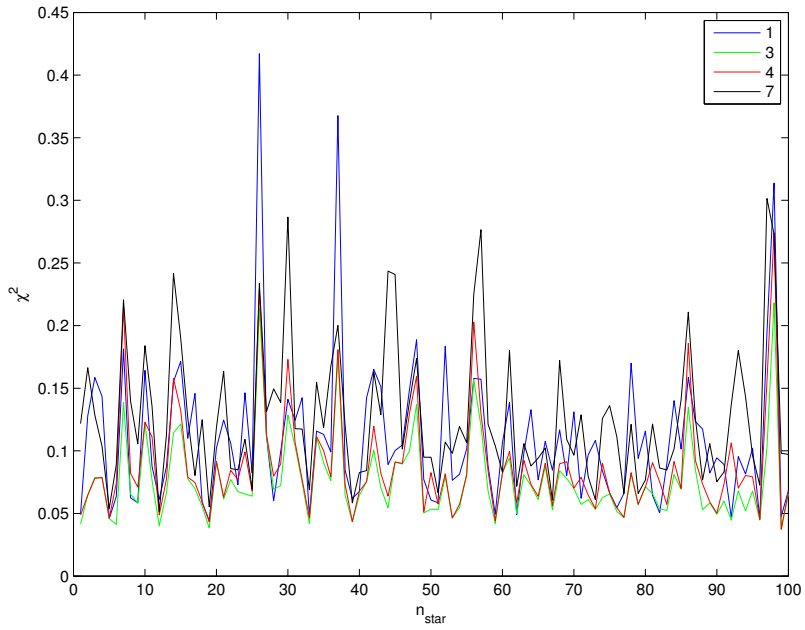

Fig. 5 The χ^2 of reconstructions by using different numbers of PCs are compared. $n_{\rm star}$ is the id of the star. The blue line corresponds to reconstructions done by only one PC. The green, red and black lines correspond to the cases of three, four and seven PCs that are used. The green line is the lowest one indicating the best fit.

realization. Finally, we compare the differences between the two, $(\delta R^2, \delta e_1, \delta e_2)$.

Figures 10, 11, 12 and 13 compare δR^2. As above, the blue, red and green lines are for the results of EMPCA, Moffatlets and Gaussianlets respectively. They show Moffatlets fit the size of stars best (the average δR^2 over 100 stars is close to 0 and the scatter is very small) and Gaussianlets did worst (the average δR^2 is always biased away from 0 although its scatter is small. As shown in Figure 2, the Gaussian function decreases too fast at a large radius, so Gaussianlets underestimate the sizes of PSFs that have large "wings"). EMPCA also does well but introduces larger scatters because of the noise in the PCs.

Figures 14, 15, 16 and 17 compare the uncertainty in ellipticity. The black dots show the ellipticity (e_1, e_2) measured from the original stars (without background noise

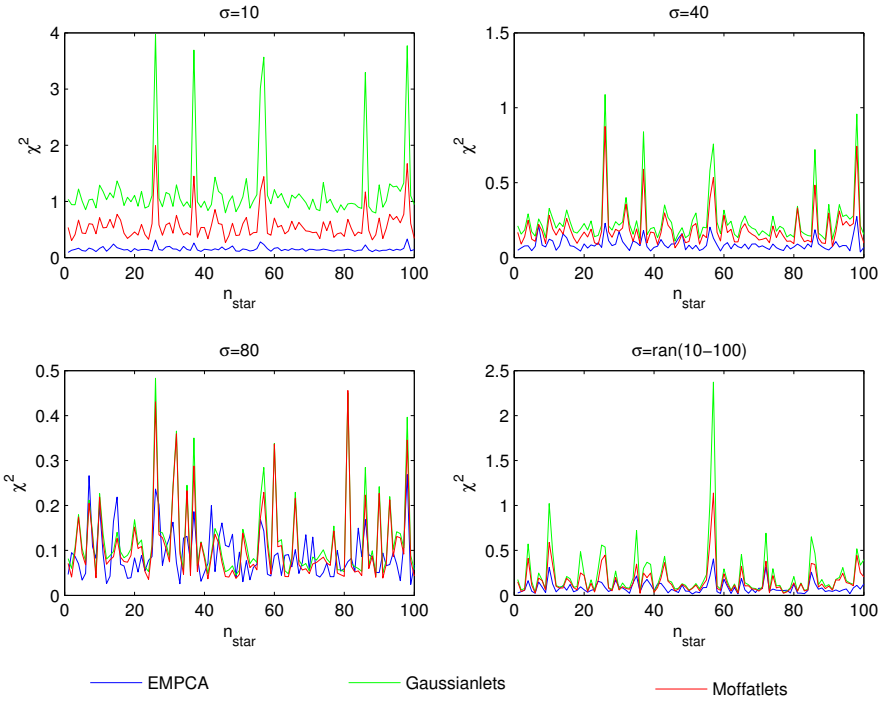

Fig. 6 χ^2-curves in the test of data set R02S01-diffraction-OFF. Blue lines are for EMPCA, green lines for Gaussianlets and red lines for Moffatlets. The same denotement is adopted in the following χ^2-plots shown in Figs. 7, 8, 9 and δR^2-plots shown in Figs. 10, 11, 12, 13.

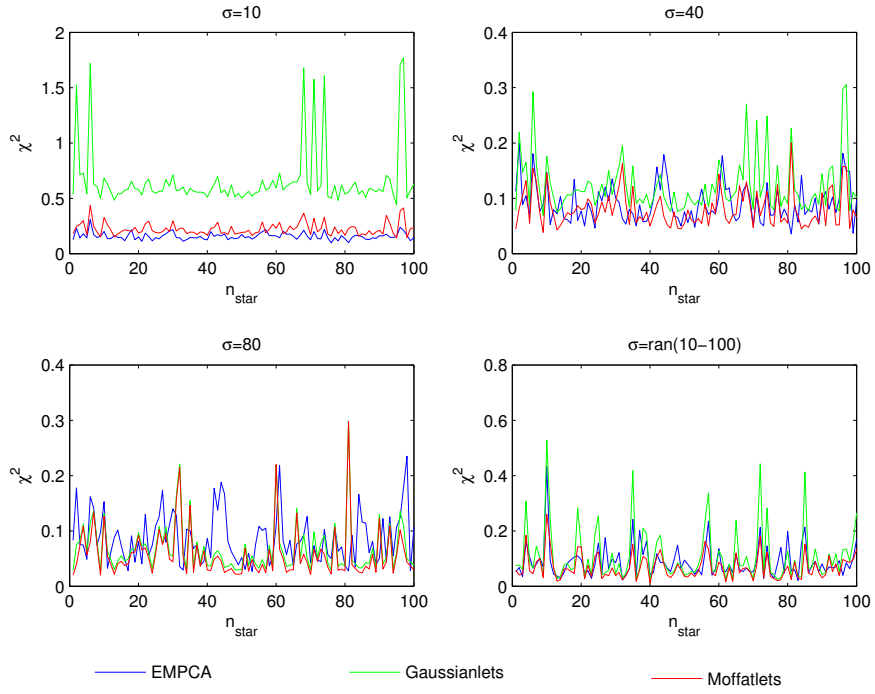

Fig. 7 χ^2-curves in the test of data set R02S01-diffraction-ON.

added yet) and the colored dots show the deviations of ellipticity $(\delta e_1, \delta e_2)$ between reconstructed stars and original stars. For the basis function methods, the ellipticity is measured first for all stars and the basis functions are then correspondingly reshaped. Therefore, the Moffatlets and Gaussianlets methods share the same ellipticity and we just plot the results of Moffatlets here. The ellipticity is measured from data where Gaussian noise is added, so when the noise increases, the scatter in ellipticity also increases.

As we can see, the basis function methods fit the ellipticity of stars much better than EMPCA. Although

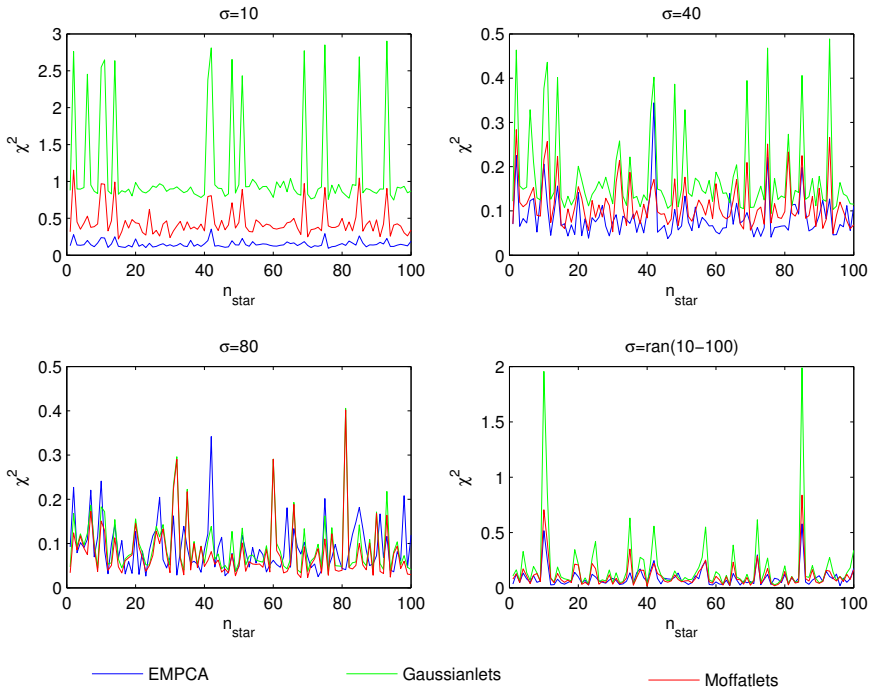

Fig. 8 χ^2-curves in the test of data set R22S11-diffraction-OFF.

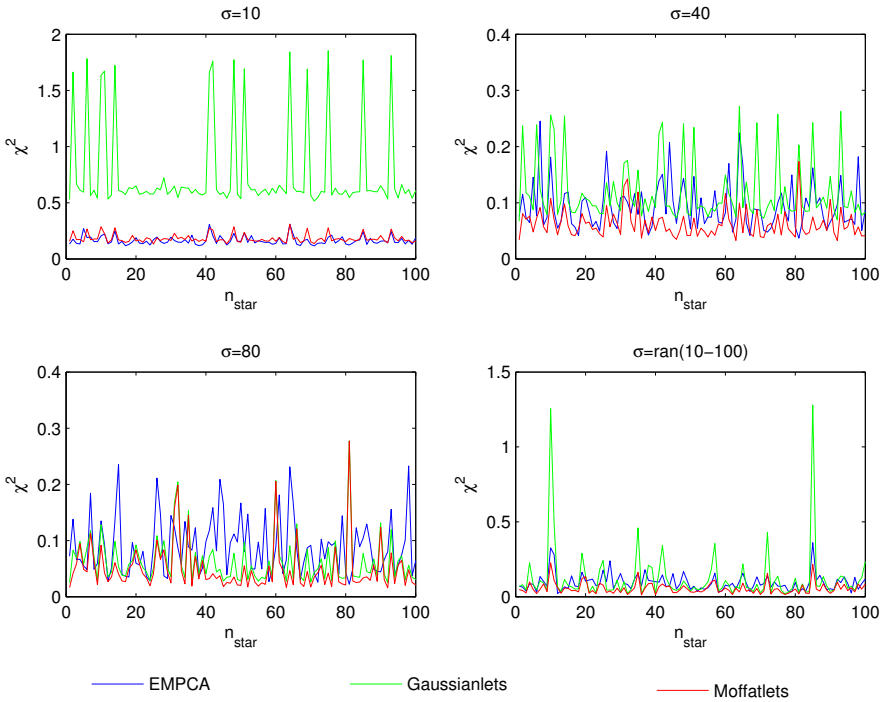

Fig. 9 χ^2-curves in the test of data set R22S11-diffraction-ON.

EMPCA performs well on the χ^2 test, it introduces larger scatters in the size, especially in the ellipticity of the PSF. This implies more stars are needed in the EMPCA method in order to reconstruct an unknown PSF's size and ellipticity to the required accuracy. We calculate σ_{R^2}/R^2 and σ_e in different simulation runs. The corresponding results are listed in Tables 3, 4, 5, 6 and 7. As shown in Paulin-Henriksson et al. (2008), uncertainties in size and ellipticity of PSF calibration are the two key parameters which will propagate into the systematics of shear measurement. The requirement for systematic bias of a cosmic shear measurement with $\sigma^2_{\rm sys} \lesssim 10^{-7}$ would be $\sigma_{R^2}/R^2 \lesssim 10^{-3}$ and $\sigma_e \lesssim 10^{-3}$. This requirement would present a ma-

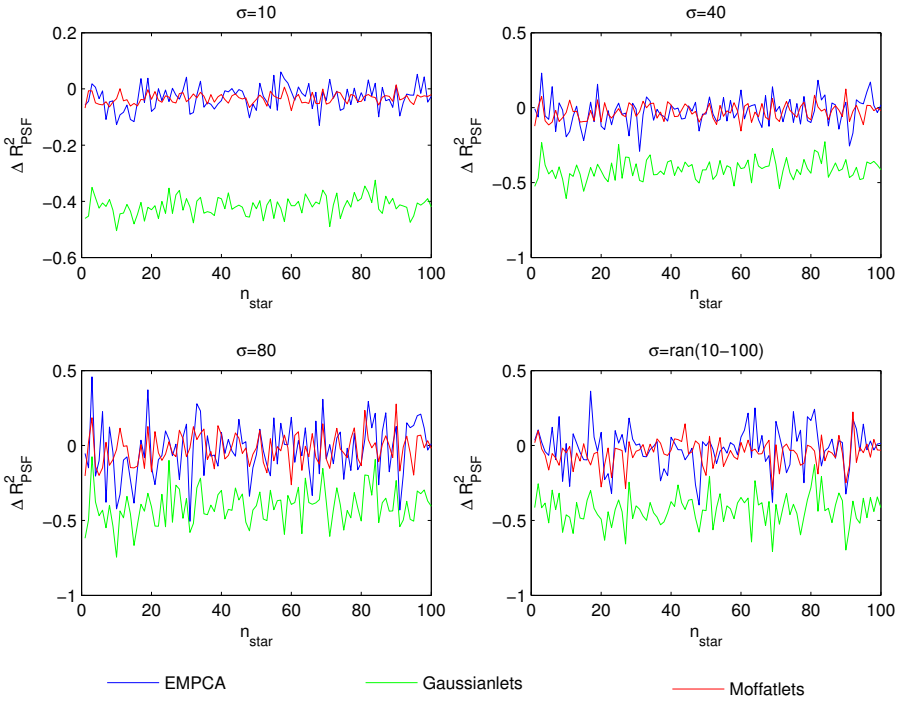

Fig. 10 δR^2-curves in the test of data set R02S01-diffraction-OFF.

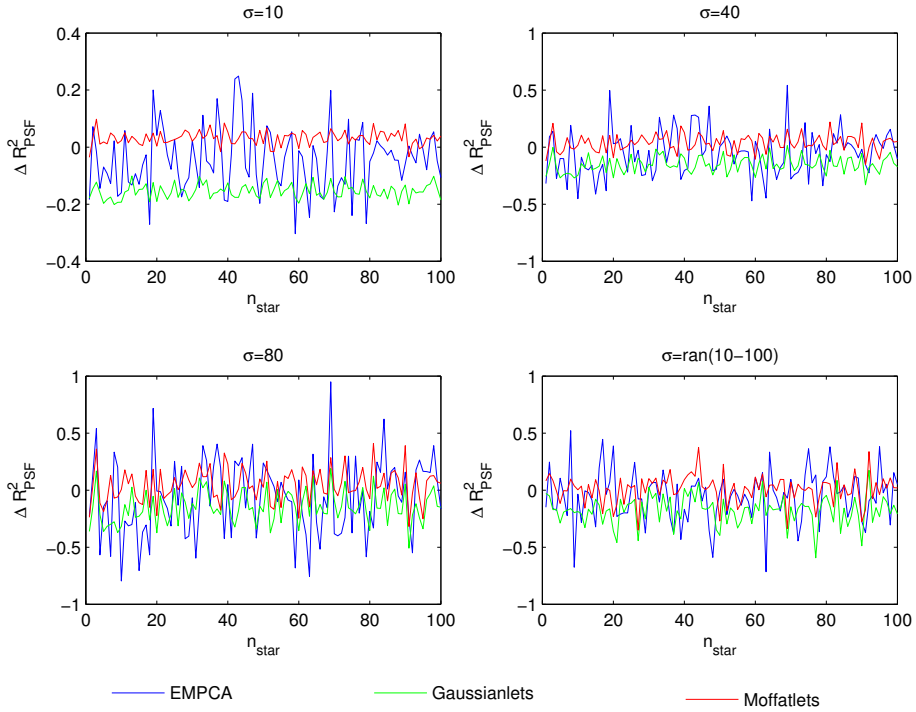

Fig. 11 δR^2-curves in the test of data set R02S01-diffraction-ON.

jor challenge for PSF reconstruction methods using PCA. Moffatlets satisfy the requirement very well, but just because no sharp spikes are present in the data. It is challenge to model sharp spikes using circularly symmetric Moffatlets.

5 CONCLUSIONS AND DISCUSSION

We use three methods to reconstruct the simulated star images. The basis function methods use smooth functions which have explicit formulas and are easy to create. As our test results have shown, Moffatlets performed better

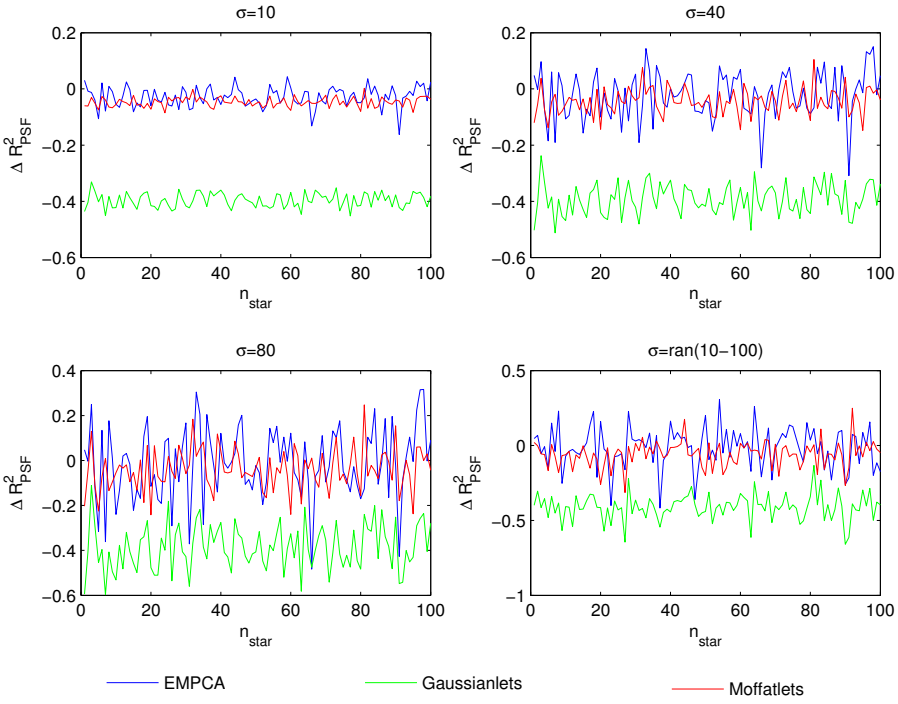

Fig. 12 δR^2-curves in the test of data set R22S11-diffraction-OFF.

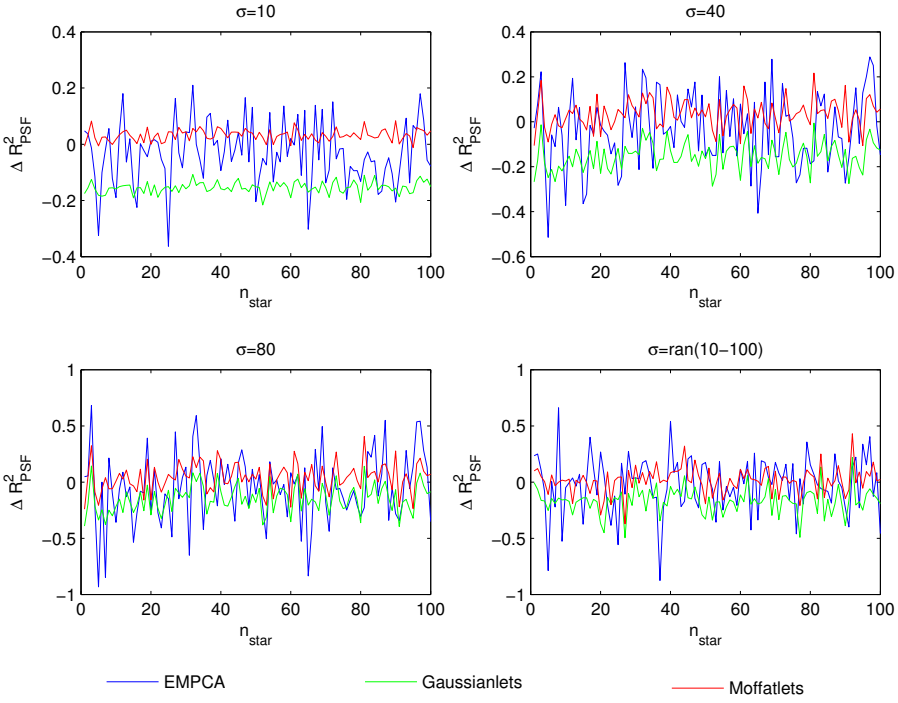

Fig. 13 δR^2-curves in the test of data set R22S11-diffraction-ON.

in image reconstructions than Gaussianlets. This is mainly because the Moffat function is a better PSF model than the Gaussian function.

Due to pixelization and finite size, our basis functions are not exactly orthogonal to each other. This will increase the cross-correlation between the coefficients. Numerical orthogonalization algorithms, such as the Gram-Schmidt process or Householder transformation, can be applied to resolve this problem. The basis function methods use circularly symmetric functions which are then shaped into elliptical ones according to the premeasured ellipticity of stars. As a result, they only consider radial variation. High-

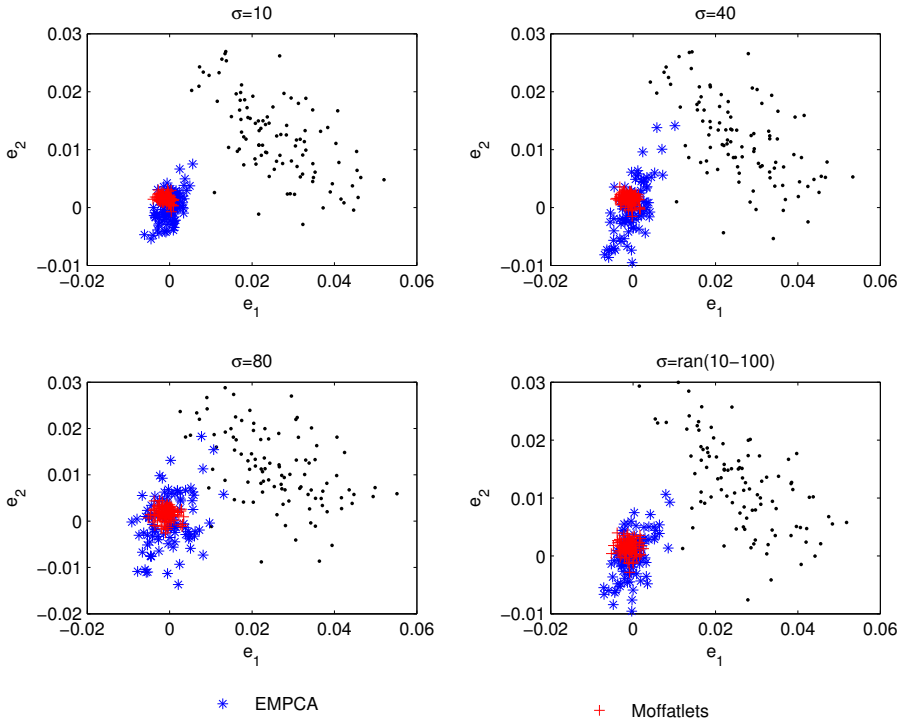

Fig. 14 $(\delta e_1, \delta e_2)$ plotted for the test of data set R02S01-diffraction-OFF. In the figure, there are two kinds of spots: black spots are ellipticity (e_1, e_2) measured from the original stars before background noise is added; colored spots (blue and red) represent the difference in ellipticity $(\delta e_1, \delta e_2)$ between the original stars and reconstructed stars using EMPCA and Moffatlets respectively. In Figs. 15, 16 and 17 we use the same color denotation.

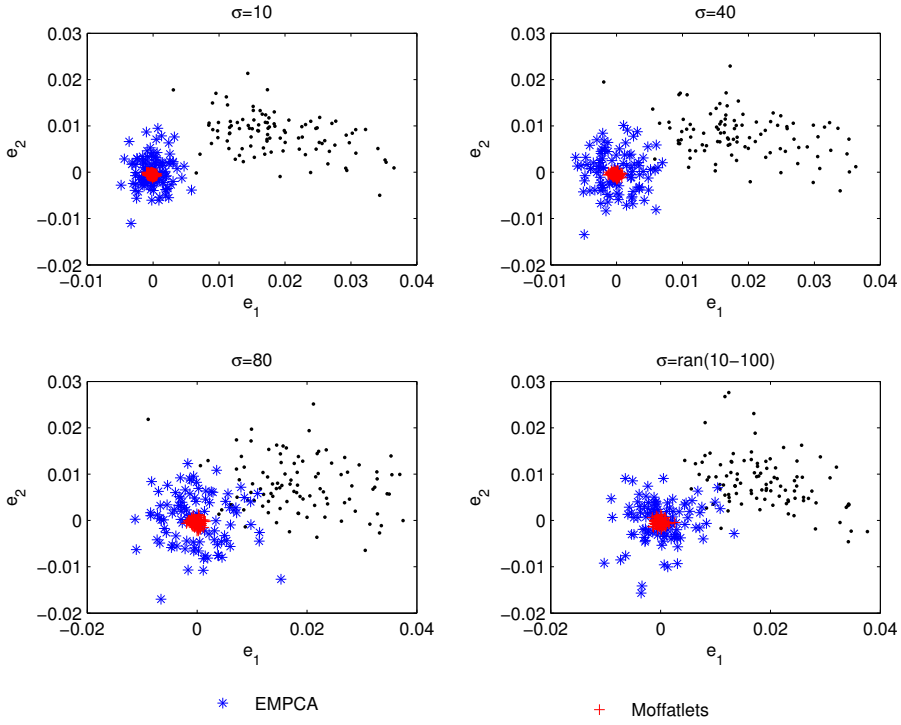

Fig. 15 $(\delta e_1, \delta e_2)$ plotted for the test of data set R02S01-diffraction-ON.

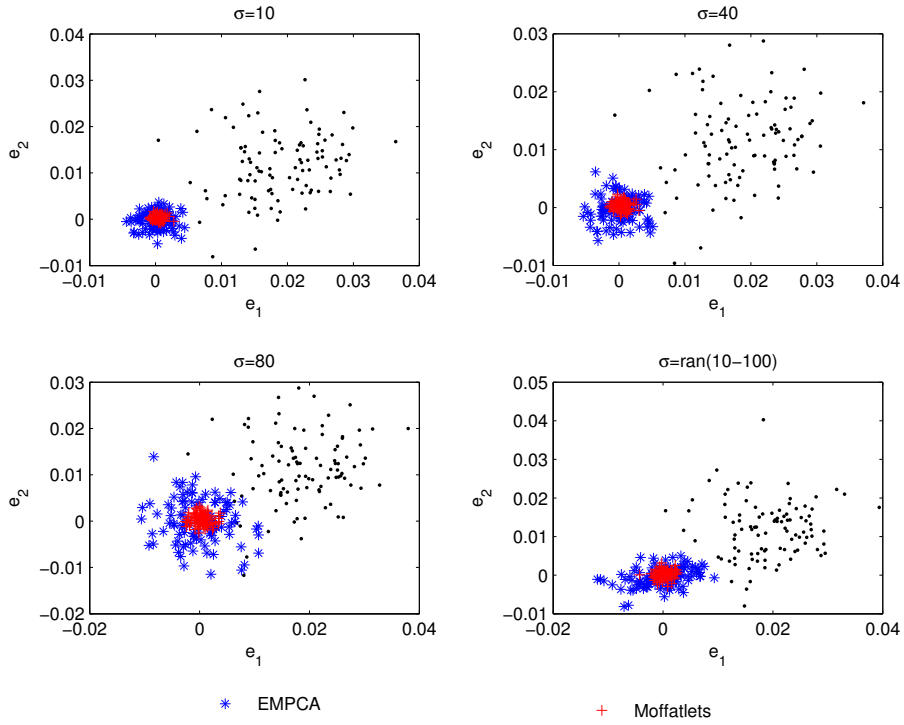

Fig. 16 $(\delta e_1, \delta e_2)$ plotted for the test of data set R22S11-diffraction-OFF.

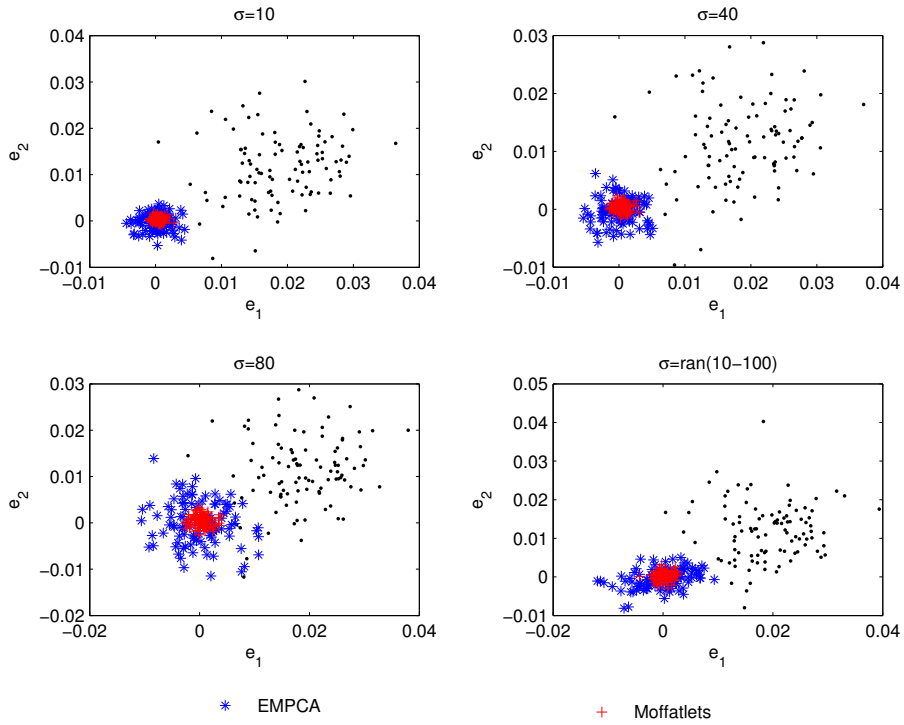

Fig. 17 $(\delta e_1, \delta e_2)$ plotted for the test of data set R22S11-diffraction-ON.

order angular structures, such as diffraction spikes, usually appear in realistic PSFs and will, in principle, introduce bias into our results. Our tests show that this is not a major issue in our simulated LSST images since the presented diffraction spikes are not very sharp and Moffatlets can be reconstructed very well, at least in terms of ellipticity and size of the PSF. More detailed studies on the issue of sharp diffraction spikes are beyond the scope of this paper.

Table 3 Value of $[\sigma_{R^2}/R^2]$ for EMPCA in Different Simulation Runs

	10	40	80	ran (10–100)
R02S01-diffraction-OFF	0.0080	0.0148	0.0280	0.0209
R02S01-diffraction-ON	0.0079	0.0136	0.0223	0.0150
R22S11-diffraction-OFF	0.0066	0.0128	0.0234	0.0198
R22S11-diffraction-ON	0.0074	0.0108	0.0201	0.0163

Table 4 Value of $[\sigma_{R^2}/R^2]$ for Moffatlets in Different Simulation Runs

	10	40	80	ran (10–100)
R02S01-diffraction-OFF	0.0058	0.0090	0.0160	0.0149
R02S01-diffraction-ON	0.0026	0.0055	0.0101	0.0081
R22S11-diffraction-OFF	0.0072	0.0093	0.0147	0.0151
R22S11-diffraction-ON	0.0024	0.0048	0.0087	0.0075

Table 5 Value of $[\sigma_{R^2}/R^2]$ for Gaussianlets in Different Simulation Runs.

	10	40	80	ran (10–100)
R02S01-diffraction-OFF	0.0635	0.0636	0.0647	0.0672
R02S01-diffraction-ON	0.0103	0.0111	0.0134	0.0142
R22S11-diffraction-OFF	0.0578	0.0576	0.0581	0.0611
R22S11-diffraction-ON	0.0100	0.0106	0.0123	0.0130

Table 6 Value of σ_e for the EMPCA method in Different Simulation Runs

	10	40	80	ran (10–100)
R02S01-diffraction-OFF	0.0018	0.0029	0.0037	0.0028
R02S01-diffraction-ON	0.0018	0.0025	0.0037	0.0035
R22S11-diffraction-OFF	0.0013	0.0017	0.0030	0.0031
R22S11-diffraction-ON	0.0016	0.0027	0.0043	0.0040

Table 7 Value of σ_e for Moffatlets/Gaussianlets in Different Simulation Runs

	10	40	80	ran (10–100)
R02S01-diffraction-OFF	0.0009	0.0010	0.0013	0.0012
R02S01-diffraction-ON	0.0004	0.0004	0.0005	0.0005
R22S11-diffraction-OFF	0.0006	0.0007	0.0009	0.0009
R22S11-diffraction-ON	0.0004	0.0004	0.0005	0.0005

The EMPCA method has several advantages over the basis function methods: (1) The resolved PCs are compact and flexible. It is the most efficient way to reconstruct irregular images. (2) The PCs are orthogonal to each other, which makes their coefficients independent and they can be easily interpolated. When using the PCA method, the resolved PCs inevitably contain noise. This would introduce relatively higher scatter in the size and ellipticity of the reconstructed PSF and then increase systematic bias in the cosmic shear measurement.

The current PSF reconstruction method is still not accurate enough to produce a satisfying shear measurement for weak lensing surveys. High-order angular structures like diffraction spikes have not been considered in detail in this paper. However, our tests have shown that Moffatelets are a very promising tool for PSF reconstruction. In future studies, we will combine the angular structures of Moffatlets and EMPCA techniques together to search for PCs in a finite Moffatlets space.

Acknowledgements BS and GL are supported by the National Key Basic Research Program of China (2015CB857000) and the "Strategic Priority Research Program the Emergence of Cosmological Structures" of the Chinese Academy of Sciences (XDB09000000). GL also thanks the supports from the One-Hundred-Talent fellowships of CAS and the National Natural Science Foundation of China (NSFC, Grant Nos. 11273061 and 11333008). BS acknowledges support from the NSFC (Grant No. 11403103). JC, JRP and WC acknowledge supports from Purdue University, the Department of Energy (DE-SC00099223), and the LSST Project (C44054L).

Appendix A: MATHEMATICAL DERIVATION OF RADIAL FUNCTIONS OF MOFFATLETS

In this appendix, we give the derivation of the radial functions of the Mofattlets, showing that the basis functions have an analytic form. We require that radial basis functions are modified by a weight function with a Moffat profile

$$Q_l(r) = R_l(r)w(r), w(r) = \left[1+\left(\frac{r}{r_d}\right)^2\right]^{-\beta}. \quad \text{(A.1)}$$

The radial basis functions satisfy

$$2\pi\int_0^{+\infty} drrR_l(r)R_{l'}(r)e^{-u(r)} = \delta_{ll'}, \quad \text{(A.2)}$$

where

$$u(r) = -\ln\left\{\left[1+\left(\frac{r}{r_d}\right)^2\right]^{-2\beta}\right\}. \quad \text{(A.3)}$$

The corresponding inverse function is

$$r = a(u) = r_d\sqrt{e^{u/2\beta}-1}\,. \quad \text{(A.4)}$$

We have

$$rdr = \frac{r_d^2}{4\beta}e^{\frac{u}{2\beta}}du. \quad \text{(A.5)}$$

Then Equation (A.2) reads

$$\frac{\pi r_d^2}{2\beta}\int_0^{+\infty} duR_l[a(u)]R_{l'}[a(u)]e^{-(1-1/2\beta)u} = \delta_{ll'}. \quad \text{(A.6)}$$

We change the variables according to $v(u) = (1-1/2\beta)u$ and introduce a new function to relate r and v in the form $r = b(v)$. Equation (A.2) reads

$$\frac{\pi r_d^2}{2\beta-1}\int_0^{+\infty} dvR_l[b(v)]R_{l'}[b(v)]e^{-v} = \delta_{ll'}. \quad \text{(A.7)}$$

We notice that this equation is similar to weighted integration of Laguerre polynomials (Eq. (4))

$$\int_0^{+\infty} dv L_l(v) L_{l'}(v) e^{-v} = \delta_{ll'}. \quad \text{(A.8)}$$

Then we have

$$R_l(r) = \sqrt{\frac{2\beta-1}{\pi r_d^2}} L_l[v(r)], \quad \text{(A.9)}$$

where

$$v(r) = \left(\frac{1}{2\beta} - 1\right) \ln\left[1 + \left(\frac{r}{r_d}\right)^2\right]^{-2\beta}. \quad \text{(A.10)}$$

The final radial basis function reads

$$Q_l(r) = \sqrt{\frac{2\beta-1}{\pi r_d^2}} L_l\Big[v(r)\Big]\left[1 + \left(\frac{r}{r_d}\right)^2\right]^{-\beta}. \quad \text{(A.11)}$$

References

Andrae, R., Melchior, P., & Jahnke, K. 2011, MNRAS, 417, 2465

Bailey, S. 2012, PASP, 124, 1015

Bartelmann, M., & Schneider, P. 2001, Phys. Rep., 340, 291

Bridle, S., Balan, S. T., Bethge, M., et al. 2010, MNRAS, 405, 2044

Hoekstra, H., Franx, M., Kuijken, K., & Squires, G. 1998, ApJ, 504, 636

Hoekstra, H., & Jain, B. 2008, Annual Review of Nuclear and Particle Science, 58, 99

Huterer, D. 2010, General Relativity and Gravitation, 42, 2177

Kaiser, N., Squires, G., & Broadhurst, T. 1995, ApJ, 449, 460

Kitching, T. D., Balan, S. T., Bridle, S., et al. 2012, MNRAS, 423, 3163

Kitching, T. D., Rowe, B., Gill, M., et al. 2013, ApJS, 205, 12

Laureijs, R., Amiaux, J., Arduini, S., et al. 2011, arXiv:1110.3193

Li, G., Xin, B., & Cui, W. 2012, arXiv:1203.0571

Li, G., Xin, B., & Cui, W. 2013, in IAU Symposium, 288, Astrophysics from Antarctica, ed. M. G. Burton, X. Cui, & N. F. H. Tothill, 306

LSST Science Collaboration, Abell, P. A., Allison, J., et al. 2009, arXiv:0912.0201

Luppino, G. A., & Kaiser, N. 1997, ApJ, 475, 20

Mandelbaum, R., Rowe, B., Bosch, J., et al. 2014, ApJS, 212, 5

Massey, R., & Refregier, A. 2005, MNRAS, 363, 197

Massey, R., Kitching, T., & Richard, J. 2010, Reports on Progress in Physics, 73, 086901

Massey, R., Hoekstra, H., Kitching, T., et al. 2013, MNRAS, 429, 661

Mellier, Y. 1999, ARA&A, 37, 127

Moffat, J. W. 2006, astro-ph/0608675

Paulin-Henriksson, S., Amara, A., Voigt, L., Refregier, A., & Bridle, S. L. 2008, A&A, 484, 67

Paulin-Henriksson, S., Refregier, A., & Amara, A. 2009, A&A, 500, 647

Peterson, J. R., Jernigan, J. G., Kahn, S. M., et al. 2015, ApJS, 218, 14

Planck Collaboration, Ade, P. A. R., Aghanim, N., et al. 2014, A&A, 571, A17

Refregier, A. 2003a, MNRAS, 338, 35

Refregier, A. 2003b, ARA&A, 41, 645

Refregier, A., & Bacon, D. 2003, MNRAS, 338, 48

Saglia, R. P., Bertschinger, E., Baggley, G., et al. 1993, MNRAS, 264, 961

Spergel, D., Gehrels, N., Baltay, C., et al. 2015, arXiv:1503.03757

Trujillo, I., Aguerri, J. A. L., Cepa, J., & Gutiérrez, C. M. 2001, MNRAS, 328, 977

Van Waerbeke, L., Benjamin, J., Erben, T., et al. 2013, MNRAS, 433, 3373